

Modal Analysis of a Two-Dimensional Oscillating Cylinder

MEAM 536 Final Project

University of Pennsylvania

Nathaniel Ruhl and Shinya Kondo

May 2022

Abstract

The sheer amount of information in fluid flows prevents efficient computation of flow parameters for active control of unwanted fluid structures. Since many fluid flows are dominated by energetic structures called coherent structures, it is often possible to capture the most important characteristics of the flow using techniques of *modal analysis*. In this investigation, we conduct CFD simulations and use two modal analysis techniques, POD and DMD, in order to extract the dominant coherent structures from the fluid flow data of a transversely oscillating cylinder. The oscillation was kept at an amplitude of $A = 0.25D$ and differing nondimensional oscillation frequencies of $f_e/f_0 = 0.5, 1.0, 1.5$ were analyzed. For all three cases, the flow was kept in the laminar regime at $Re = 100$. Through this analysis, we retrieved the dominant spatial structures and the associated frequencies of the cylinder wake, and identified that for $f_e/f_0 < 2$, the frequency of the dominant spatial mode always decreases. By comparing the spatial and temporal characteristics, we identified a linear relationship between the spatial size and frequency of the dominant modes. Using the dominant spatial and temporal characteristics identified in the modal analysis, we created reduced-order models of the velocity flow fields. While the reconstruction for the stationary cylinder correctly captured both the spatial and temporal characteristics of the flow, the reconstruction for the oscillating cylinder only captured the temporal characteristics. This shows that reduced-order modelling of non-periodic structures in time are not suitable for generalized Fourier series expansion.

This report also investigates the mechanism behind the formation of the von Karman vortex street in the wake of an oscillating cylinder. A qualitative analysis of vorticity contour plots concludes that a cylinder's oscillation prevents the shedding of vortices at the natural frequency of the vortex street behind a stationary cylinder. We infer that the delay in vortex shedding due to the forced oscillation is caused by an increase in dynamic pressure on the leading edge of the cylinder's motion. Future investigations include a quantitative investigation of this phenomenon, and a more accurate reduced-order modelling of the flow behind an oscillating cylinder.

1 Introduction

Fluid flows with seemingly simple geometries and parameters can often exhibit colorful complex flow structures due to nonlinearities, instabilities, and turbulence. These complexities result in dense flow data that becomes increasingly difficult to comprehend as parameters become more complex. Because of this, many researchers are developing mathematical tools to extract energetically and dynamically important features of the fluid flow. These techniques are called modal analysis techniques. Modal analysis techniques are used by researchers and engineers to extract dominant coherent structures of the fluid flow in order to create simplified models of the complex dynamics called “reduced-order models” (ROMs) [12]. Reduced-order models created through these procedures are strongly desirable since they can model the dynamics at the fraction of the computational cost of running a full simulation.

External flows over bluff bodies exist in many engineering applications around us. The flow over a car, an airfoil, or even a building can be modelled as flow over bluff bodies in different Reynolds number regimes. Due to their prevalence in engineering applications, the flow over bluff bodies is a highly researched field in fluid dynamics. Namely, the von Karman vortex street that forms as a result of the flow over a circular cylinder is one of the most highly researched phenomena [6]. While most classical studies investigate the flow

around a stationary cylinder, many real world flows modelled as flow around a cylinder involve movement of the cylinder. If these kinematics are not properly accounted for in the simplified “toy model” of the flow over a cylinder, the model may not produce reliable results. This is vital in structural engineering where unwanted resonance with the von Karman vortex streets may cause the collapse of a building, failure in pipes along the ocean floor, or even the collapse of street lights [1].

Understanding the formation and interference of wake structures behind a bluff body can be used to reduce drag, increase mixing or heat transfer, and enhance combustion [9]. Vortex shedding can be altered by either making passive modifications to the flow geometry and/or providing a steady forcing to the system. Roshko (1955) [11] placed a splitter plate behind the cylinder in order to prevent transverse motion of the fluid, which in turn suppressed vortex shedding. Park et. al. (1994) [9] created a feedback control system consisting of a single sensor and a pair of blowing/suction actuators. Park et. al. (1994) achieved complete suppression of vortex shedding for $Re = 60$, and only partial suppression for $Re = 80$ [9]. In this investigation, we will see that the forced transverse oscillation of a cylinder also has the potential to control unwanted vortical structures in the cylinder wake.

We conduct numerical simulations of a flow behind a stationary and transversely oscillating cylinder using the software package, ANSYS Fluent. The oscillating cylinder has an amplitude of $A = 0.25D$ with three different frequency ratios of $f_e/f_0 = 0.5, 1.0, 1.5$. For all test cases, the flow is kept in the laminar regime with $Re = 100$. To further investigate the coherent flow patterns behind each configuration, different modal analysis techniques will be applied to the simulation data. The resulting reduced-order models are analyzed to report the coupling mechanism between the movement of the cylinder and its affect on the structures behind the cylinder.

This report will be organized as follows. Sec. 2 describes past investigations of the flow behind a transversely oscillating cylinder, while Sec. 3 details the derivation of the modal decomposition techniques that will be used in this investigation. Sec. 4 details the steps of the numerical investigation in ANSYS Fluent. The results from the numerical simulation and modal decomposition are reported in Sec. 5 along with discussions of the results. Finally, the paper is concluded in Sec. 6, and Appendix B provides a link to simulations, data, and code for all of the analysis presented in this report.

2 Literature Review and Motivation

Oseen’s equations provide an analytical solution to the flow around a two-dimensional disc at low Reynolds numbers, but this solution only applies for steady flows below a critical value of $Re_c \approx 46$ [2]. The Karman vortex streets that appear in the regime of $46 \lesssim Re \lesssim 188$ are steady and two-dimensional [2]. In his review of vortex dynamics in the cylinder wake, Williamson (1996) [15] calls this the “laminar vortex shedding regime”. The upper limit of this laminar regime has been widely studied in order to better understand the onset of discontinuities and the transition to three-dimensional vortex structure [15]. The laminar vortex shedding regime is well-understood as compared to other Reynolds number regimes for the flow over a stationary cylinder, and a number of analytical solutions have been proposed to describe the steadily translating vortex street [15]. However, the laminar regime has not garnered much attention for an oscillating cylinder, which will be the focus of this investigation.

There are three dimensionless quantities that determine the flow structure behind a transversely oscillating cylinder. The first is the Reynolds number, $Re = UD/\nu$, where U is the inlet velocity, D is the characteristic diameter of the cylinder, and ν is the kinematic viscosity of the fluid. The second is the ratio A/D which compares the amplitude of the cylinder’s oscillation, A , to the cylinder’s diameter, D , and the third is the ratio f_e/f_0 where f_e is the forced oscillation frequency of the cylinder and f_0 is the natural vortex-shedding frequency of a stationary cylinder. Ongoren and Rockwell (1988) [8] conducted flow-visualization experiments in the range of $584 \leq Re \leq 1300$ and studied the phase of vortex formation in the near wake, as well as vortex-vortex interaction in the von Karman vortex street for different frequency ratios. For frequency ratios near $f_e/f_0 \sim 1.17$, they found that the phase of the vortex shedding changes by 180° . This has important implications when considering the vortex-induced forces on the cylinder, as the direction of the forces can change drastically in a narrow range of forced oscillation frequencies [3].

In terms of vortex-vortex interactions in the vortex street, Ongoren and Rockwell (1988) found that at $f_e/f_0 = 1.0$, there is an increase in the transverse spacing and coherence of the vortices [8]. Building off

the experimental results of Ongoren and Rockwell (1988), Blackburn and Henderson (1998) conducted two-dimensional simulations at $Re = 500$ and $A/D = 0.25$ to further study the mechanical energy transferred from the flowing fluid to the cylinder, which is determined by the phase of vortex shedding, as well as the time-periodic structures of the vortex street [3]. However, since $Re = 500$ approaches the turbulent regime in which the cylinder wake exhibits three-dimensional behavior, they concluded the two dimensional simulations are inadequate to describe the full nature of vortex shedding [10]. For this reason, Ping et. al. (2021) conducted three-dimensional simulations at $Re = 500$, $A/D = 0.25$, and $0.5 \leq f_e/f_0 \leq 1.5$ to further explore the hypotheses proposed by Blackburn and Henderson (1998) [3]. The three-dimensional numerical study showed that the phase switch at $f_e/f_0 = 1.0$ is a result of the competition between surface-acceleration and pressure-gradient vorticity production mechanisms. Furthermore, the modal analysis technique, Dynamic Mode Decomposition (DMD) was carried out to further elucidate the coupling mechanism between the natural shedding frequency of the von Karman vortex streets and the forced oscillation due to the displacement of the cylinder.

In this report, we consider the steady, two-dimensional regime of laminar vortex shedding. Similar to Blackburn and Henderson (1998) and Ping et. al. (2021), we consider $A/D = 0.25$. We conducted four simulations, one of the flow past a stationary cylinder, and the other three for the frequency ratios of $f_e/f_0 = 0.5, 1$, and 1.5 , each for $Re = 100$. We use DMD to characterize the growth and decay of temporal structures within the cylinder's wake for both vorticity and velocity fields, and use a Fourier transformation of the coefficient of lift as an alternative method to identify the dominant frequency of the von Karman vortex streets.

3 Theory of Modal Analysis

Modal decomposition is a mathematical technique used to extract energetically dominant features of dynamical systems. The two data-driven methods described in this section are the Proper Orthogonal Decomposition (POD) and the Dynamic Mode Decomposition (DMD). There are multiple other data-driven and operator-driven modal decomposition techniques, many of which have been developed based on the fundamental concepts of POD and DMD. Taira et. al. (2017) [5], Rowley (2017) [12], and Taira et. al. (2020) [6] provide excellent reviews of the major modal decomposition techniques used in fluid dynamics.

3.1 Proper Orthogonal Decomposition

The Proper Orthogonal Decomposition (POD), also commonly referred to as Principal Component Analysis (PCA) in other fields of science and engineering, was first introduced to the fluid dynamics community by Lumley (1967) [7] to understand the complex dynamics of turbulent flows. In general, POD reduces the dimensionality of the flow data by creating a low-order approximation that only contains the energetically dominant basis vectors [5].

As noted by Rowley (2017), it is often advantageous to represent data by an affine space (a shifted subspace) [12]. In POD, a velocity field $\mathbf{u}(\mathbf{x}, t)$ is separated from its temporal mean $\bar{\mathbf{u}}(\mathbf{x})$ to isolate the unsteady component of $\mathbf{u}(\mathbf{x})$. The “fluctuation” of the velocity field has the Fourier series expansion

$$\mathbf{u}(\mathbf{x}, t) - \bar{\mathbf{u}}(\mathbf{x}) = \sum_j a_j(t) \phi_j(\mathbf{x}, t) \quad (1)$$

where $\phi_j(\mathbf{x}, t)$ are orthogonal “spatial modes” and $a_j(t)$ are coefficients that represent the strength of a spatial mode at a given time.

If $X \in \mathbb{R}^{n \times m}$ is a data matrix that contains m time snapshots of data column vectors $\mathbf{x}(t) \in \mathbb{R}^n$, then the covariance matrix (representing the kinetic energy of the fluctuations: $KE = \int u'^2 dV$) is

$$R = XX^T \in \mathbb{R}^{n \times n}. \quad (2)$$

The spatial modes, ϕ_j , are given by the eigenvectors of the covariance matrix

$$R\phi_j = \lambda_j \phi_j, \quad \phi_j \in \mathbb{R}^n. \quad (3)$$

The eigenvalues are naturally ordered from largest to smallest; therefore, the corresponding eigenvectors represent the dominant spatial modes of the flow. Since the velocity vectors are real, the eigenvectors are necessarily real and must come in pairs to capture symmetric spatial wavenumber modes of the flow. To isolate the phase and amplitude of the flow, other methods such as Spectral POD (SPOD) and DMD can be used.

3.1.1 The Method of Snapshots

The first method to calculate the spatial modes, ϕ_j , is to directly solve eigensystem of the spatial covariance matrix in Eq. (3). However, if the number of spatial nodes, n , is much larger than the number of time steps, m , then the $n \times n$ matrix R is very large, and it is computationally inefficient to calculate and store, in both memory and time. For this reason, the ‘‘Method of Snapshots’’ is a practical alternative method for calculating POD modes. The Method of Snapshots was introduced in 1987 by Sirovich [14], and relies on solving a smaller eigenvalue problem for the temporal covariance matrix (or in general for non-fluid applications, column-wise covariance matrix). The temporal covariance matrix is

$$T = X^T X \in \mathbb{R}^{m \times m}, \quad (4)$$

and the temporal modes, ψ_j , are the eigenvectors of the temporal covariance matrix

$$T\psi_j = \lambda_j \psi_j, \quad \psi_j \in \mathbb{R}^m \quad (5)$$

As discussed by Taira et. al. (2017) [5], once the eigenvectors ψ_j are solved, the spatial eigenvectors (POD modes) can be recovered by

$$\phi_j = X\psi_j \frac{1}{\sqrt{\lambda_j}}, \quad j = 1, 2, \dots, n. \quad (6)$$

3.2 Singular Value Decomposition

As discussed in Sec. 3.1, there are multiple ways to compute the most energetic modes for POD. The most direct method is to apply an eigenvalue decomposition directly to the covariance matrix $R = XX^T$. In order to reduce the computational cost of this procedure, the Method of Snapshots was introduced, in which the covariance matrix $T = X^T X$ is decomposed into its eigenvalues and eigenvectors. Although these two methods provide important insight into POD, the most common method in practice to solve for POD modes is the Singular Value Decomposition.

The Singular Value Decomposition (SVD) is a generalization of eigenvalue decomposition for rectangular matrices [5]. The eigendecomposition of vector $\mathbf{v}_j \in \mathbb{R}^n$ is given by

$$B\mathbf{v}_j = \lambda_j \mathbf{v}_j \quad (7)$$

where $B \in \mathbb{C}^{n \times n}$ is a square matrix that stretches the vector \mathbf{v}_j by the eigenvalue λ_j . On the other hand, the SVD is described by

$$A\mathbf{v}_j = \sigma_j \mathbf{u}_j \quad (8)$$

where the matrix $A \in \mathbb{C}^{n \times m}$ is a rectangular matrix that maps a *right-singular vector* $\mathbf{v}_j \in \mathbb{R}^m$ into a *left-singular vector* $\mathbf{u}_j \in \mathbb{R}^n$, which lives in a different dimensional vector space and is scaled by the *singular value* σ_j . The SVD can be written in matrix form as

$$AV = U\Sigma \quad (9)$$

where $V \in \mathbb{C}^{m \times m}$ and $U \in \mathbb{C}^{n \times n}$ are unitary matrices whose columns contain the left and right singular vectors respectively, and $\Sigma \in \mathbb{R}^{n \times m}$ contains p singular values along its diagonal where $p = \min(n, m)$. Left-multiplying each side of Eq. (9) by $V^{-1} = V^*$, we arrive at the governing equation of the SVD:

$$A = U\Sigma V^*. \quad (10)$$

In conclusion, SVD is different from eigenvalue decomposition because eigendecomposition is used for square matrices. In SVD, since A is a rectangular matrix, two sets of basis vectors are needed to describe its domain and codomain, which are V and U respectively.

3.2.1 Relationship between SVD and POD Covariance Matrices

The SVD of the data matrix X can be written directly as

$$X = \Phi \Sigma \Psi^T, \quad (11)$$

where $\Phi \in \mathbb{R}^{n \times n}$, $\Psi \in \mathbb{R}^{m \times m}$, and $\Sigma \in \mathbb{R}^{n \times m}$ contains the singular values. The columns of Φ , the right-singular vectors of X , contain the spatial POD modes $\phi_j \in \mathbb{R}^n, j = 1, \dots, n$, and the columns of Ψ , the right-singular vectors of X , contain the temporal POD modes $\psi_j \in \mathbb{R}^n, j = 1, \dots, m$. These observations can be encapsulated in the following eigenvector equations

$$(XX^T)\Phi = \Phi \Sigma^2 \quad (12)$$

$$(X^T X)\Psi = \Psi \Sigma^2. \quad (13)$$

3.3 Dynamic Mode Decomposition

The Dynamic Mode Decomposition (DMD) is a data-driven method that reduces high-order data to a reduced-order linear model by extracting both spatial and temporal coherent structures [5]. Since DMD is purely a data-driven method, it has wide range of applicability, as it does not require knowledge of the dynamics underlying a system [6]. Let $X = [\mathbf{x}_1 \dots \mathbf{x}_{m-1}] \in \mathbb{R}^{n \times m-1}$ be a data matrix where the column vectors $\mathbf{x}_m \in \mathbb{R}^n$ represent $m - 1$ snapshots in time, and the matrix $X' = [\mathbf{x}_2 \dots \mathbf{x}_m] \in \mathbb{R}^{n \times m-1}$ be the data matrix advanced one step forward in time. The main assumption behind DMD is that there is a linear operator, $A \in \mathbb{C}^{n \times n}$ which propagates the system forward in time:

$$\mathbf{x}_{j+1} = A\mathbf{x}_j, \quad \mathbf{x}_j \in \mathbb{R}^n, \quad j = 1, \dots, m - 1. \quad (14)$$

The DMD approximates the eigenvalues and eigenvectors of A and orders them in terms of importance. To reduce the computational cost of deriving the eigenvalues and eigenvectors of the full matrix A , we can compute a reduced linear operator \tilde{A} using the following steps. First, compute the SVD of X , from which the dominant coherent spatial structures, or SVD “modes”, are given by the columns of U . The next step is to project A onto the column vectors of $U \in \mathbb{R}^{n \times m-1}$. This step creates a reduced order linear operator $\tilde{A} \in \mathbb{C}^{m-1 \times m-1}$:

$$\tilde{A} = U^* A U = U^* X' V \Sigma^{-1}. \quad (15)$$

The reduced operator, \tilde{A} , has the eigendecomposition $\tilde{A}W = W\Lambda$. The eigenvectors of the original A matrix, which are given by the columns of Φ , are equal to

$$\Phi = X' V \Sigma^{-1} W. \quad (16)$$

For highly periodic flows that are well captured by only a few modes, a reduced DMD can be defined in which $r < m - 1$ columns of U are used when constructing \tilde{A} , such that $\tilde{A} \in \mathbb{R}^{r \times r}$. Let the complex eigenvalues of \tilde{A} be $\lambda_j, j = 1, \dots, r$. The frequency, f_j , and the growth rate, g_j , corresponding to the j 'th mode are given by

$$f_j = \log(\text{Im}(\lambda_j)) / 2\pi\Delta t, \quad (17)$$

$$g_j = \log(\text{Re}(\lambda_j)) / 2\pi\Delta t \quad (18)$$

where Δt is the time-step of the simulation data.

When conducting DMD analysis, it is not conventional to subtract out the temporal mean of fluid flow from the column vectors \mathbf{x}_j (which is done in POD analysis). This is important because when DMD is

computed for an oscillating cylinder, the temporal mean of the velocity field is not well-defined, since the fluid domain changes based on the cylinder's location at every time step. Additionally, it is important to note that DMD has been observed to exhibit sensitivities and yield biased results when the data contains significant measurement uncertainties [6]. Therefore, when analyzing experimental data with DMD, users should be aware of sensor accuracy and should consider "noise-robust" variants of DMD [6].

3.4 Modal Reconstruction

The POD and DMD procedures described in this section are essentially a spectral decomposition of the flow data matrix [13, 10]. Using the eigenvectors as the spatial modes and the eigenvalues as the temporal properties of each mode, the entire flow field can be reconstructed using

$$X = \sum_{j=1}^{m-1} \phi_j \lambda_j. \quad (19)$$

Since the bulk of the energy of the flow can be captured using the first r modes, a low order representation of the flow can be approximated by

$$X_{approx} \approx \sum_{j=1}^r \phi_j \lambda_j^{p-1} \alpha_j, \quad (20)$$

where the power $p = 1, 2, \dots, m - 1$ on the eigenvalues are included to account for the contribution (linear dependence) of the residual $m - r - 1$ eigenvectors. The extra complex amplitude α_j is included in order to adjust the relative importance of each spatial mode when r modes are used in the approximation of Eq. (19), and is also strongly related to the system's response to initial conditions and the time interval over which the data is collected [13]. Eq. (20) can be written in matrix form as

$$[\mathbf{x}_1 \ \mathbf{x}_2 \ \dots \ \mathbf{x}_{m-1}] \approx [\phi_1 \ \phi_2 \ \dots \ \phi_r] \begin{bmatrix} \alpha_1 & & & \\ & \alpha_2 & & \\ & & \ddots & \\ & & & \alpha_r \end{bmatrix} \begin{bmatrix} 1 & \lambda_1 & \dots & \lambda_1^{m-2} \\ 1 & \lambda_2 & \dots & \lambda_2^{m-2} \\ \vdots & \vdots & \ddots & \vdots \\ 1 & \lambda_r & \dots & \lambda_r^{m-2} \end{bmatrix} \quad (21)$$

$$X_{approx} \approx \Phi D_\alpha V_{and} \quad (22)$$

By using only the first r dominant modes, we assume that the remaining $m - r - 1$ modes are linearly dependent of the first r modes, which is provided in the use of the Vandermonde matrix in the last term of Eq. (21).

The weights α_j are used to match the low-order approximation of the flow to the full flow data, which are computed by solving the minimization problem

$$\underset{\boldsymbol{\alpha}}{\text{minimize}} \quad J(\boldsymbol{\alpha}) = \|X - X_{approx}\|_F \quad (23)$$

$$\underset{\boldsymbol{\alpha}}{\text{minimize}} \quad J(\boldsymbol{\alpha}) = \|U\Sigma V^* - \Phi D_\alpha V_{and}\|_F \quad (24)$$

$$\underset{\boldsymbol{\alpha}}{\text{minimize}} \quad J(\boldsymbol{\alpha}) = \|\Sigma V^* - W D_\alpha V_{and}\|_F, \quad (25)$$

where $\|\cdot\|_F$ is the Frobenius norm of a matrix.

By solving for the complex amplitudes α_j , $j = 1, \dots, r$, within the diagonal matrix D_α that solve the above minimization problem, the flow can be reconstructed using the r dominant modes to create a reduced-order model (ROM).

4 Problem Formulations

4.1 Governing Fluid Equations

In our numerical simulation, the incompressible Navier-Stoke's Equations were solved. These equations can be written as

$$\frac{\partial \mathbf{u}}{\partial t} + (\mathbf{u} \cdot \nabla) \mathbf{u} = -\frac{1}{\rho} \nabla p + \nu \nabla^2 \mathbf{u}, \quad (26)$$

$$\nabla \cdot \mathbf{u} = 0. \quad (27)$$

In this equation, \mathbf{u} is the velocity field, ρ is the fluid density, ν is the fluid's kinematic viscosity, and p is the fluid pressure.

4.2 ANSYS Simulation Setup

The simulation software ANSYS Fluent was used to conduct the numerical simulations of each flow configuration. Figure 5 shows the domain and mesh used in the study. The two-dimensional domain is $30D \times 35D$ where D is the diameter of the cylinder. A refinement zone of size $8D \times 20D$ was created around the cylinder to more accurately capture the von Karman vortex streets. A hexagonal-dominant mesh was used with an element size of $0.0025D$ right around the cylinder, a maximum element size of $0.1D$ in the refinement zone and $0.3D$ around the entire domain. The resulting discretized domain had approximately 40,000 elements. The applied boundary conditions are no shear on the top and bottom edges, as well as no-slip on the cylinder circumference. There was a inlet velocity to maintain $Re = 100$ on the left side of the domain, and a pressure outlet on the right edge.

The cylinder was displaced using a user-defined displacement equation

$$y = A \sin(2\pi f_e t) \quad (28)$$

where A is the amplitude of oscillation and f_e is the frequency of oscillation. This equation was implemented using C++. The dynamic meshing was used to remesh the domain after each time step when the cylinder moved.

The governing equations were solved using a second order implicit time scheme. The implicit scheme is unconditionally stable; therefore, the time step does not affect the stability of the solution. In the POD analysis done by Taira et. al. (2020) [6], 325 snapshots of the flowfield behind a stationary sphere are used in order to observe eight vortex-shedding periods. Based on visual inspection of flow behind a stationary cylinder with $Re = 100$, it takes about $t = 1$ (non-dimensionalized) for the von-Karman vortex street to form and ~ 0.5 for eight vortex shedding periods to occur. In this study, we first ran the stationary cylinder case for $t = 2$ (non-dimensionalized) before collecting 500 snapshots of data with $\Delta t = 0.005$.

4.3 The Strouhal Number

The Strouhal number is a non-dimensional frequency that is used to characterize the frequency, f , of the vortex street, behind a cylinder. The Strouhal number is given by

$$St = \frac{fD}{U} \quad (29)$$

where D is the diameter of the cylinder and U is the inlet velocity. The Strouhal number will be calculated to characterize the oscillations of each mode in the wakes of the stationary and oscillating cylinders.

5 Results and discussion

All movies of the simulation results from ANSYS can be found in Appendix B. Though not necessary, it is recommended that the reader watches each video first before delving into the analysis of the proceeding sections as the visual component will help the reader follow each discussion.

5.1 Stationary Cylinder

5.1.1 Fourier Analysis

The lift coefficient C_L is a dimensionless number that characterizes the lift force on a body and is proportional to the circulation of the vortices. Taking advantage of this property, oscillation frequency of the vortex formations can be computed by taking the Fourier Transform of the time varying lift coefficient.

The time variation of the lift coefficient, C_L , for the stationary cylinder can be found in Fig. 6. This time signal can be used to determine the frequency of the vortex shedding by taking its discrete Fast Fourier Transform (FFT). The results of this process can be found in Fig. 6, which indicate that the natural shedding frequency of the stationary cylinder is $St = 0.1414$.

5.1.2 POD Analysis

The POD analysis of the flow behind a stationary cylinder was conducted using the SVD method. The data matrix for the velocity field was created as explained in Sec. 3. Data column vectors at each timestep contains the streamwise velocity field stacked ontop of the spanwise velocity field, such that if there are n nodes in the CFD domain the size of a single data column is $2n^2 \times 1$. SVD was carried out on the data matrix in order to visualize the most energetic spatial modes. Fig. 14, depicts the 20 largest singular values. Since σ^2 represents the energy contained in each Fourier mode, this shows that only the first 6 modes are required to capture $\sim 95\%$ of the total energy content of the flow. The spatial structures of the velocity magnitude of the first, third, and fifth singular modes can be found in Figures 15, 16 and 17, respectively. Visually, the first spatial mode, which contains the bulk of the flow energy, represents the spatial structures of the vortex shedding. Subsequently, the third and fifth modes are harmonics, integer multiple frequencies, of the primary vortex structures and contain less energy. As explained in Sec. 3, each mode comes in pairs due to the symmetry of the spatial wavenumbers; therefore, the second, fourth and sixth modes are equivalent to the first, third and fifth mode respectively.

5.1.3 DMD Analysis

DMD analysis was performed on the flow behind a stationary cylinder to capture the most energetic spatial modes, as well as the frequencies and growth rates of the most energetic modes. The velocity magnitude of the first, second and fourth dominant spatial modes can be found in Fig. 2. As expected, the dominant spatial modes from the DMD analysis correlate exactly with the POD spatial modes found in the previous section. The only caveat is that the DMD mode numbering is shifted by one since the first DMD mode depicts the mean velocity profile, which is subtracted from the POD analysis. The first seven dominant frequencies can be found in Fig. 1. The first dominant frequency represents the frequency of the mean velocity profile, which is zero. The first frequency pair represents the natural shedding frequency of $St = 0.14286$ and subsequent pairs are harmonics of the first pair. As expected, this correlates to the natural shedding frequency computed in the previous Fourier Analysis section, where the natural shedding frequency was found to be $St = 0.1414$. The direct correspondence between DMD spatial modes and DMD frequency to POD modes and Fourier frequency confirms that DMD analysis is capable of accurately computing the spatial and temporal characteristics of the coherent structures found in the flow data.

5.2 Oscillating Cylinder

As carried out with the stationary cylinder case, the Fourier and DMD analysis will be applied to each of the frequency ratios for the flow behind a transversely oscillating cylinder. Note that the POD analysis is not carried out for the oscillating cylinder because a proper temporal average cannot be defined to separate the temporal dependence from the flow data.

5.2.1 Fourier Analysis

The time signals of the Lift Coefficient for $f_e/f_0 = 1.0, 1.5, 0.5$ can be found in Figures 7,8 and 9 respectively. Carrying out the Fourier analysis of the time signal shows that the shedding frequencies are $St = 0.0808$ for

$f_e/f_0 = 1.0$, $St = 0.1010$ for $f_e/f_0 = 1.5$ and $St = 0.0404$ for $f_e/f_0 = 0.5$. The Fourier analysis can be found in Figures 11, 12 and 13.

5.2.2 DMD Analysis

Similar to the DMD results found in the stationary cylinder case, the DMD analysis was carried out to determine the spatial structures and temporal frequency of the dominant coherent structures. The resulting spatial structures of the first, second and fourth dominant modes can be found in Figures 19, 20, and 21 for $f_e/f_0 = 1.0$; Figures 22, 23, and 24 for $f_e/f_0 = 1.5$; Figures 25, 26, and 27 for $f_e/f_0 = 0.5$. The corresponding dominant frequencies for each of the coherent structures are provided in Figure 18 where the dominant frequencies are computed to be $St = 0.07143$ for $f_e/f_0 = 1.0$, $St = 0.10715$ for $f_e/f_0 = 1.5$ and $St = 0.03572$ for $f_e/f_0 = 0.5$.

5.2.3 Reduced-Order Model

Given the linear operator A that depicts the time evolution of the data, the eigenvectors of A represent the spatial coherent structures of the flow and the eigenvalues represents the temporal characteristics of the coherent structures (growth/decay rates and frequency). Using the minimization algorithm described in Sec. 3.4, the dominant modes of each case can be used to create a reduced-order model of the flow. Figure 4 shows the singular values of the first 20 dominant modes of each case. The square of the singular values, σ^2 , represents the energy contained in each spatial model; therefore, the number of modes required to represent $\sim 95\%$ of the total energy is 7 for the stationary cylinder and about 17 for each of the oscillating cylinder cases. The animations produced of the reduced-order models can be found in Appendix B. For the stationary cylinder case, the reduced order model retains the proper shapes and frequencies of the von Karman vortex shedding, but the shedding process is less smooth compared to the full simulation. Nevertheless, the animation is able to properly capture the dominant dynamics, which is adequate for the purpose of controlling unwanted vortex structures and resonance with control systems. On the other hand, the reduced-order models for the oscillating cylinders are able to properly capture the frequency of vortex street, but distort the spatial structures. Even though the flow is periodic in nature, without accounting for the moving cylinder at each location, Fourier reconstruction becomes difficult. To circumvent this issue, orthogonality of the modes can be enforced by keeping the center of the oscillating cylinder as the origin at each time step and describe the spatial locations using this reference coordinate system.

5.3 Comparison of stationary and oscillating cylinder

In both the Fourier and DMD analysis, the dominant frequencies are computed for each oscillating cylinder case. By comparing the dominant frequency of the oscillating cylinder of $f_e/f_0 = 1.0$ with that of the stationary cylinder, it can be seen that the dominant frequency is half of the natural shedding frequency. By comparing the spatial structures of the oscillating and stationary (Figures 15 and 20), it can be seen that the size of the dominant vortex is in the oscillating cylinder case is twice of that found in the stationary case.

Similar analysis can be carried out for the two other oscillating cases. For the case in which $f_e/f_0 = 1.5$, the dominant frequency is 3/4ths of the natural shedding frequency and the size of the dominant vortex is 4/3rds that of the stationary cylinder. For the case in which $f_e/f_0 = 0.5$, the dominant frequency is 1/4th the natural shedding frequency and the size of the dominant vortex is 4 times that of the stationary cylinder. This relationship can be seen within each mode pairing of Figure 18, which plots the Strouhal number against mode number.

It is evident that there is a pattern between the vortex shedding frequency, $f_{oscillation}$ and the frequency ratio of the cylinder's transverse oscillation, f_e/f_0 . The frequency relation is

$$f_{oscillation} = \frac{1}{2} \left(\frac{f_e}{f_0} \right) \times f_0, \quad (30)$$

This equation implies that for $f_e/f_0 < 2$, $f_{oscillation} < f_0$, but it also provides information about vortex size in the wake. Taylor's hypothesis states that the convective velocity can be approximated as the temporally averaged mean velocity at that location. Since the mean velocity of the flow is constant for $Re = 100$,

the spatial structures and temporal characteristics can be related by

$$f_0 \lambda_0 = f_{oscillation} \lambda_{oscillation} \quad (31)$$

where λ_0 and $\lambda_{oscillation}$ represent the diameter of the vortices for the stationary and oscillating cylinders respectively. Re-arranging Eq. (31), we arrive at a relationship between the ratio of shedding-vortex size and the cylinder's oscillation frequency ratio:

$$\left(\frac{\lambda_0}{\lambda_{oscillation}} \right) = \frac{1}{2} \left(\frac{f_e}{f_0} \right). \quad (32)$$

Therefore, for $f_e/f_0 < 2$, $\lambda_{oscillation} > \lambda_0$. In this particular investigation, the relations in Eqns. (30) and (32) are derived for a flow of $Re = 100$ and for frequency ratios of $f_e/f_0 = 0.5, 1.0, 1.5$. Since Taylor's hypothesis holds for both the laminar and turbulent regimes, we expect that this relation will hold for a much wider range of Reynolds numbers and frequency ratios.

As shown in Figure 18, the vortical structures and frequency of higher DMD modes are simply harmonics of the first dominant modes. Therefore, the spatial structures and frequencies of these higher modes also follow Eqns. (30) and (31), which emphasizes the validity of the derived relations.

5.3.1 Analysis of fluid-structure interaction

Modal analysis techniques highlight the dominant spatial modes and frequencies of flows, but seldom provide physical interpretation of the mechanism behind the formation of the von Karman vortex streets. In this section, we provide a qualitative description of the vortex formation based on the vorticity contour plots from the simulation data.

In the stationary cylinder case, the vortex contour for the first 0.1s can be found in Figure 28. From the figure, it can be seen that the von Karman vortex street formations the side of the cylinder where the separation occurs switches between top and bottom. This occurs because the shedding of the vortices causes that side of the cylinder to decrease in pressure, which leads to a preference for the flow to head in that direction. This is the switching mechanism which causes the von Karman vortex shedding in the stationary flow.

For the f_e/f_0 oscillating cylinder case, the vorticity contour for the first 0.2s can be found in Figure 29 and 30. The figure depicts that at the same Reynolds number as the stationary cylinder flow, there is a natural tendency for the flow to separate when the cylinder reaches the center of the wall normal direction. The shedding is prevented by the movement of the cylinder, which causes this delay in vortex shedding. This describes why for all three oscillating cases, the shedding frequency of the vortex structures decrease.

6 Conclusion

The von Karman vortex streets are infamous for bluff body flows and can be found in many engineering flow problems. Due to the simplicity of the vortex shedding pattern, its investigation has piqued the interests of researchers and engineers alike. In this investigation, the flow around a transversely oscillating cylinder at different frequency ratios are compared with the flow around a stationary cylinder to research the effects of the oscillation on the formation of the von Karman vortex streets. We used two different modal analysis techniques to extract the coherent structures of the flow to describe the spatial and temporal characteristics of each flow pattern.

The Dynamic Mode Decomposition (DMD) technique was shown to properly capture the dominant spatial modes and their temporal characteristics by comparing its results with that from Fourier analysis (which captures the temporal characteristics) and the Proper Orthogonal Decomposition (which capture the spatial coherent structures). The results confirm that DMD analysis is a combination of POD analysis and Fourier analysis. Furthermore, results of DMD analysis show that forced oscillations of $f_e/f_0 < 2$ decrease the oscillation frequency of modal structures in the wake (Eq. 30), which has potential applications in feedback control of the bluff body wake. Using Taylor's hypothesis, we derived a linear relationship between the size of the vortex structures and their shedding frequencies (Eq. 31). DMD was also used to reconstruct a reduced-order model (ROM) of each flow analyzed. While the ROM for the stationary case showed correct

spatial and temporal structures, the ROMs for the oscillating cylinder cases only capture the proper temporal characteristics, even though a larger number of modes was retained in the modal reconstruction.

The last goal of this report was to provide a qualitative description of the mechanism behind the formation of the von Karman vortex street behind a transversely oscillating cylinder. Investigating the vorticity contour of each case, it was concluded that the oscillating cylinder prevents the shedding of vortices at the natural frequency of the flow behind a stationary cylinder. For frequency ratios of $f_e/f_0 < 2$, vortex formation is delayed because there is an increase in pressure on the side of the cylinder which leads the cylinder's oscillatory motion.

In this investigation, we considered a one sided energy transfer from the solid to the fluid. In more realistic engineering problems, there is a response from the fluid to the solid called vortex induced vibrations (VIV). In future studies, we hope to investigate VIV and its effects on the von Karman vortex streets. The analysis conducted here was purely in the laminar regime but we expect the physical flow patterns to still hold in the turbulent regime. Further investigation at higher Re could be carried out to test the validity of this investigation in more realistic flow configurations.

References

- [1] Blevins, R. D. *Flow-Induced Vibration*; Van Nostrand Reinhold, 1990.
- [2] Barkley, Dwight. Linear analysis of the cylinder wake mean flow. *EPL (Europhysics Letters)* 75, no. 5: 750, 2006.
- [3] Blackburn H.M. and Henderson R.D. A study of two-dimensional flow past an oscillating cylinder. *Journal of Fluid Mechanics*, 385: 255 - 286, 1990.
- [4] Brunton, S.L., Kutz, N.J. Data-Driven Science and Engineering: Machine Learning, Dynamical Systems, and Controls. *Cambridge University Press*, 2019.
- [5] Taira, K., Brunton, S., Dawson, S.T., Rowley C.W., Colonius, T., McKeon, B.J., Schmidt, O.T., Gordeyev, S., Theofilis, V., and Ukeiley, L.S. Modal Analysis of Fluid Flows: An Overview. *AIAA Journal*, 55, 12, Dec. 2017.
- [6] Taira, K., Hemati, M.S., Brunton, S., Sun, Y., Duraisamy, K., Bagheri, S., Dawson, S.T., Yeh, C.A. Modal Analysis of Fluid Flows: Applications and Outlook *AIAA Journal*, 58, 3, March 2020.
- [7] Lumely, J.L. The structure of inhomogeneous turbulent flows. *Proceedings of the International Colloquium on the Fine Scale Structure of the Atmosphere and Its Influence on Radio Wave Propagation*, 1967.
- [8] Ongoren, A., and Rockwell, D. (1988). Flow structure from an oscillating cylinder Part 1. Mechanisms of phase shift and recovery in the near wake. *Journal of Fluid Mechanics*, 191, 197-223.
- [9] Park, D. S., Ladd, D. M., and Hendricks, E. W. Feedback control of von Kármán vortex shedding behind a circular cylinder at low Reynolds numbers. *Physics of fluids*, 6(7), 2390-2405, 1994.
- [10] Ping, H., Zhu, H., Zhang, K., Zhou, D., Bao, Y., Xu, Y., and Han, Z. Dynamic mode decomposition based analysis of flow past a transversely oscillating cylinder. *Physics of Fluids*, 33(3), 033604, 2021.
- [11] Roshko, A. On the wake and drag of bluff bodies. *Journal of the aeronautical sciences*, 22(2), 124-132, 1955.
- [12] Rowley, C. W., and Dawson, S. T. Model reduction for flow analysis and control. *Annual Review of Fluid Mechanics*, 49, 387-417, 2017.
- [13] Jovanović, M. R., Schmid, P. J., and Nichols, J. W. Sparsity-promoting dynamic mode decomposition. *Physics of Fluids*, 26(2), 024103, 2014.
- [14] Sirovich, L. Turbulence and the dynamics of coherent structures. I. Coherent structures. *Quarterly of applied mathematics*, 45(3), 561-571, 1987.

- [15] Williamson, C. H. Vortex dynamics in the cylinder wake. *Annual review of fluid mechanics*, 28(1), 477-539, 1996.
- [16] Zebib A. Stability of viscous flow past a circular cylinder. *Journal of Engineering Mathematics*, 21: 155 - 165, 1987.

A Figures

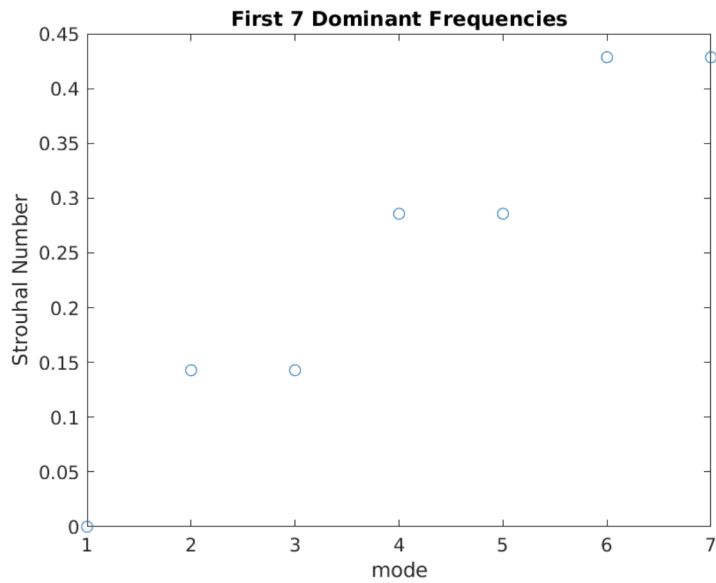


Figure 1: Strouhal number of the first 7 modes for flow around a stationary cylinder.

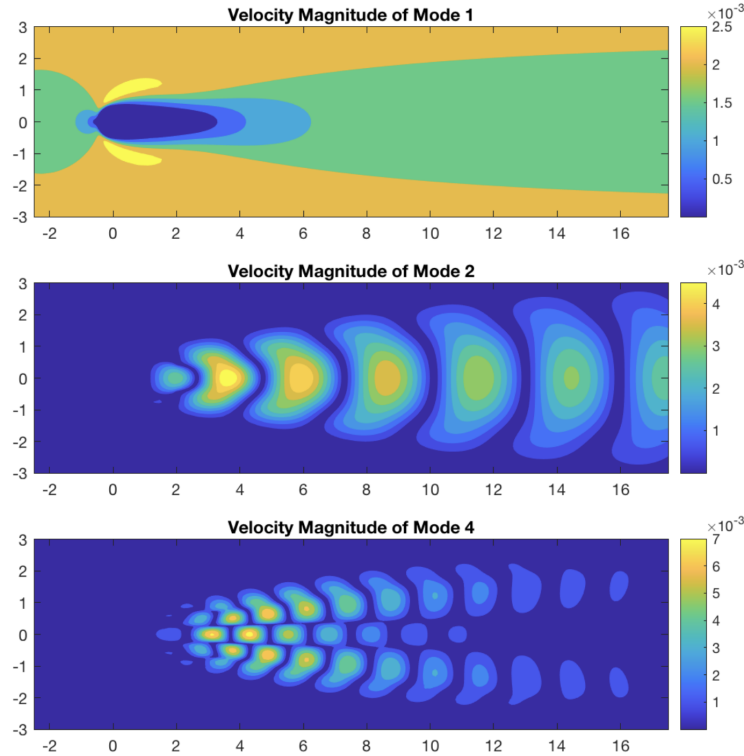


Figure 2: Spatial modes 1, 2, and 4 for the stationary cylinder.

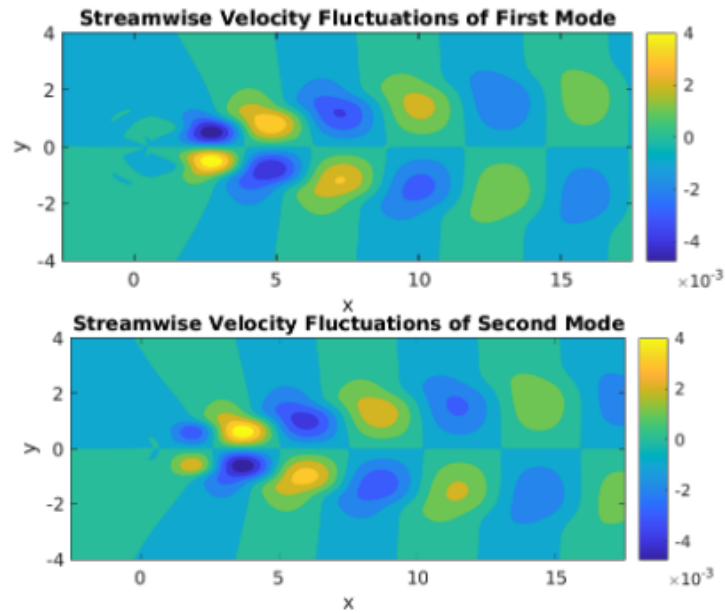


Figure 3: Streamwise Velocity Fluctuations of the first and Second POD modes. Note that the POD modes subtract the mean flow.

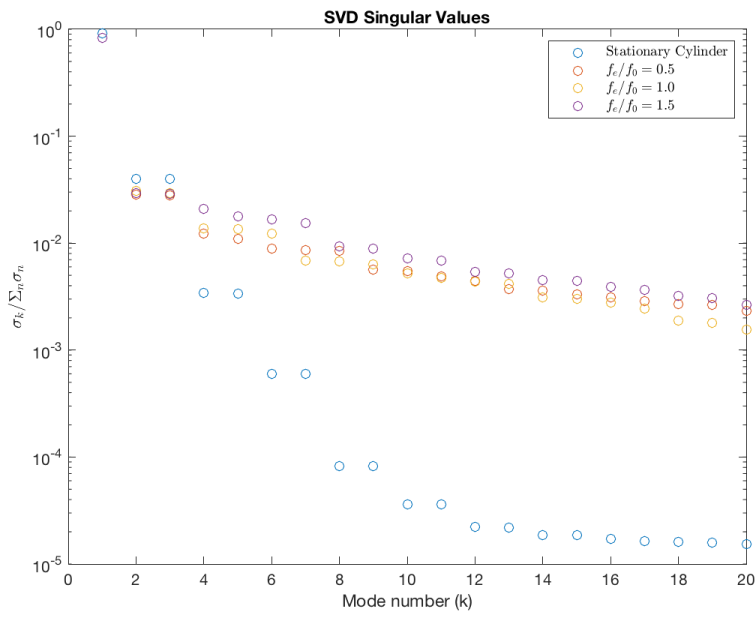


Figure 4: SVD singular values for the stationary and oscillating cylinders

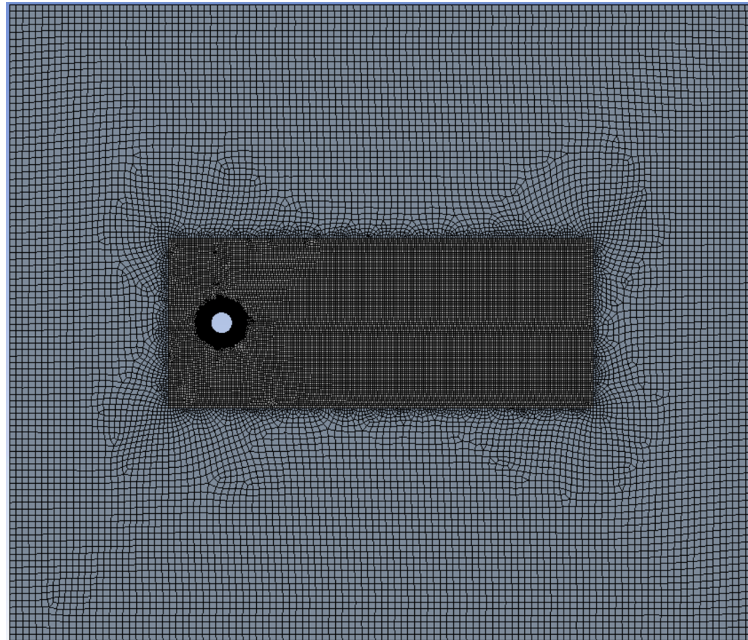


Figure 5: ANSYS mesh grid for the stationary cylinder simulation

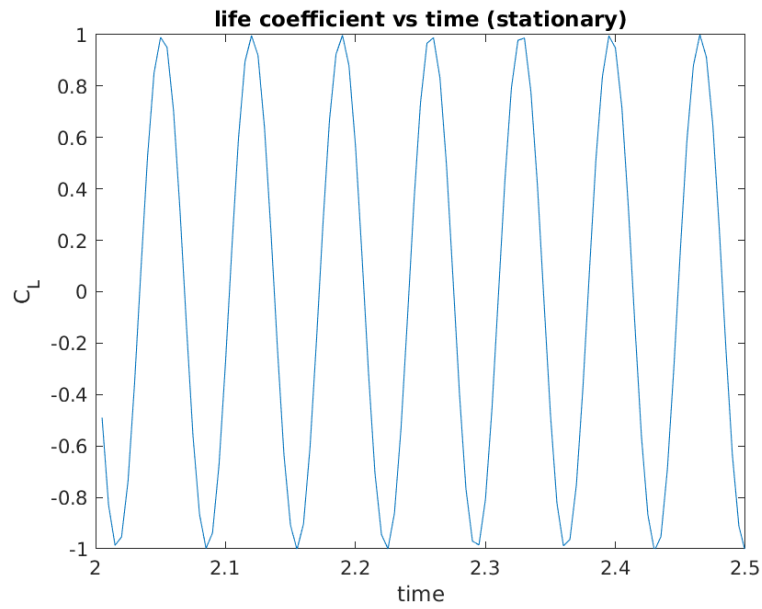


Figure 6: Time variation of lift coefficient for stationary case

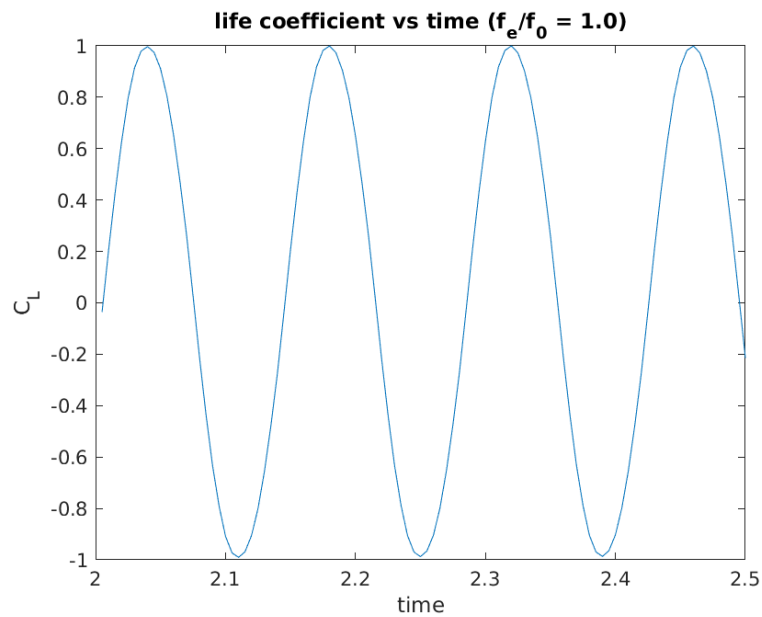


Figure 7: Time variation of lift coefficient for $f_e/f_0 = 1.0$ case

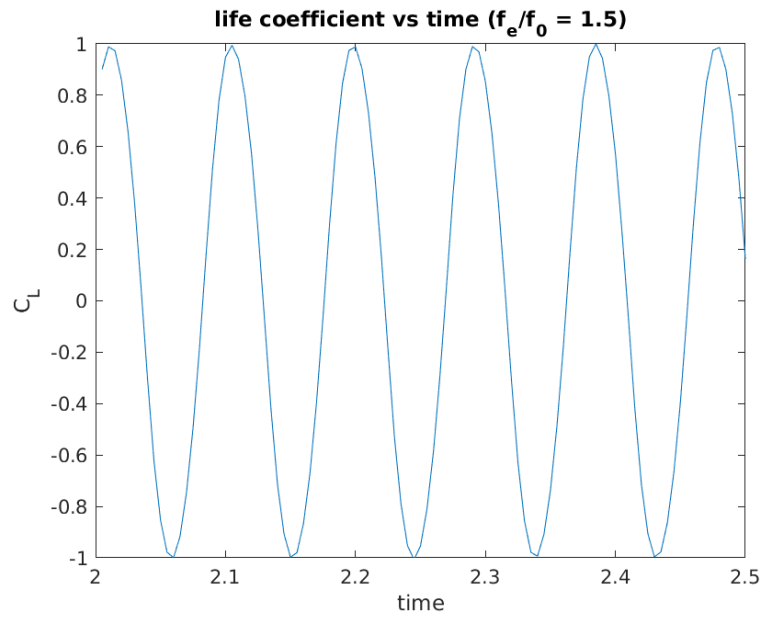


Figure 8: Time variation of lift coefficient for $f_e/f_0 = 1.5$ case

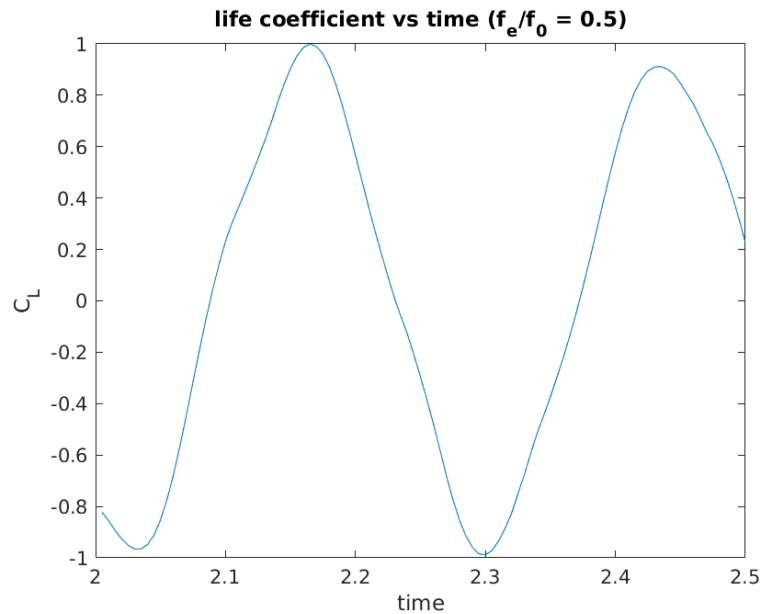


Figure 9: Time variation of lift coefficient for $f_e/f_0 = 0.5$ case

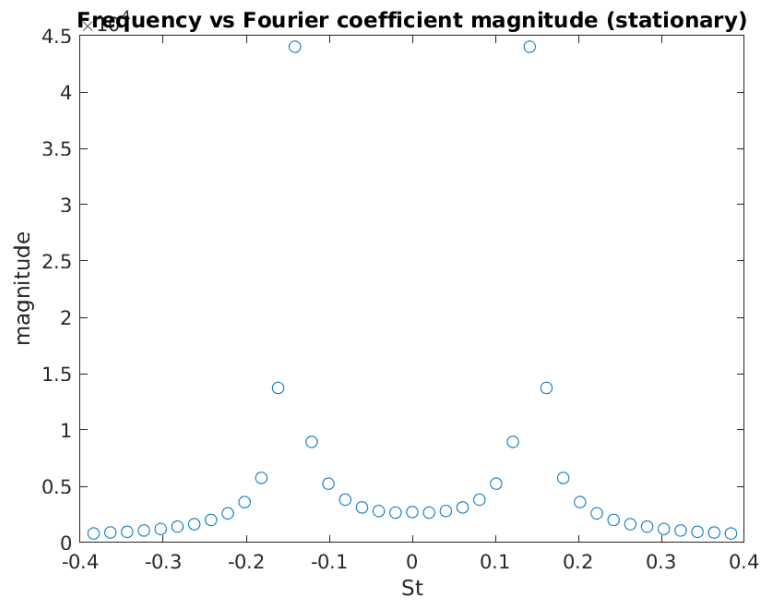


Figure 10: Frequency vs Fourier Coefficient magnitude of C_L for stationary case (Peak at $St = 0.1414$)

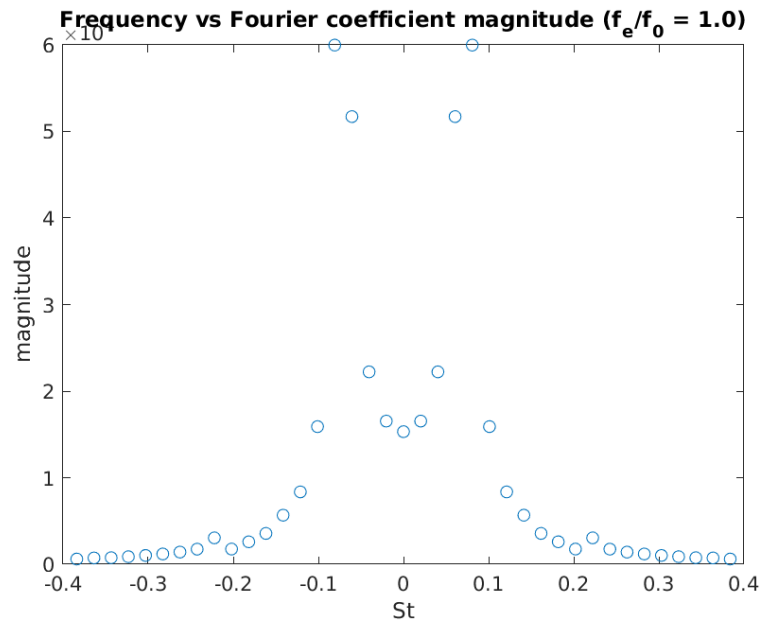


Figure 11: Frequency vs Fourier Coefficient magnitude of C_L for $f_e/f_0 = 1.0$ case (Peak at $St = 0.0808$)

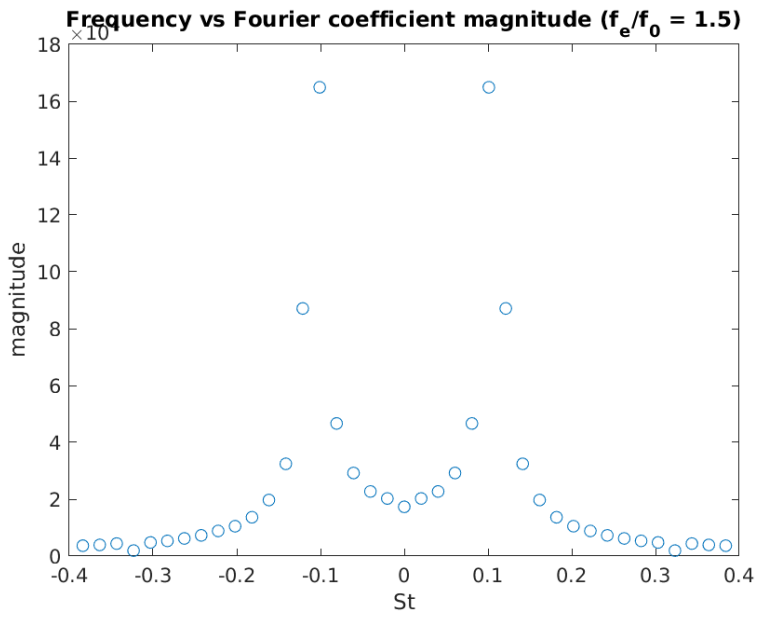


Figure 12: Frequency vs Fourier Coefficient magnitude of C_L for $f_e/f_0 = 1.5$ case (Peak at $St = 0.1010$)

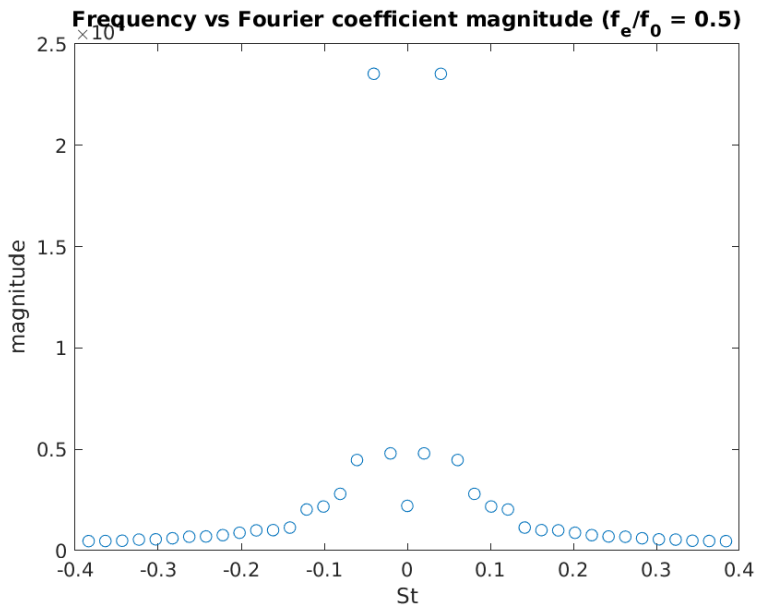


Figure 13: Frequency vs Fourier Coefficient magnitude of C_L for $f_e/f_0 = 0.5$ case (Peak at $St = 0.0404$)

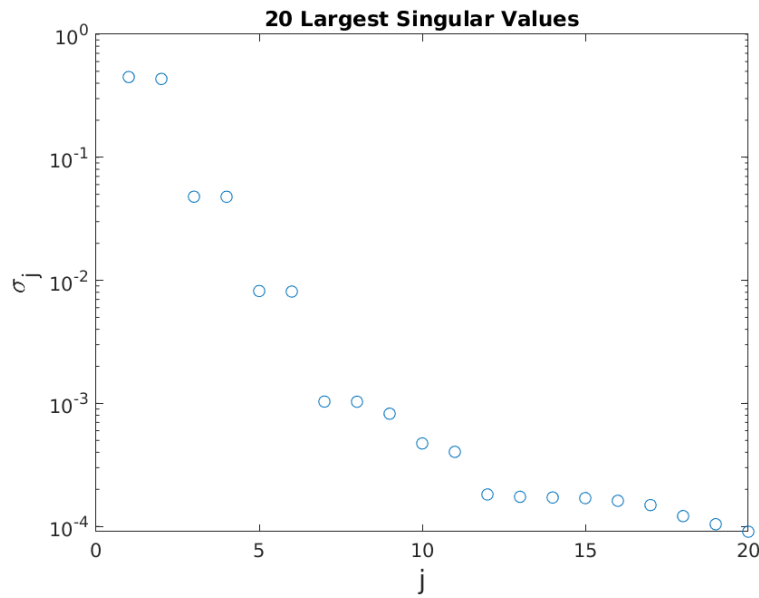


Figure 14: The 20 largest singular values from the POD analysis of the stationary cylinder flow

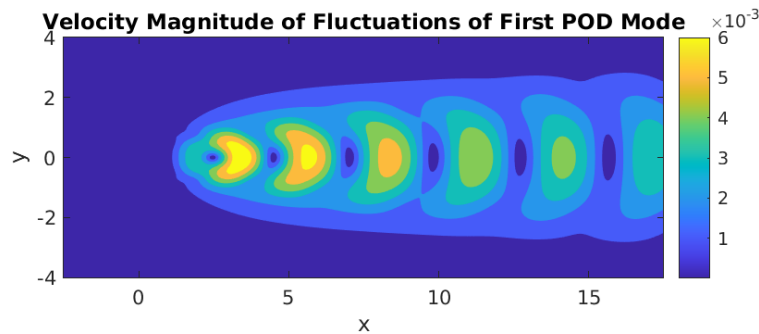


Figure 15: First spatial POD mode for the stationary cylinder

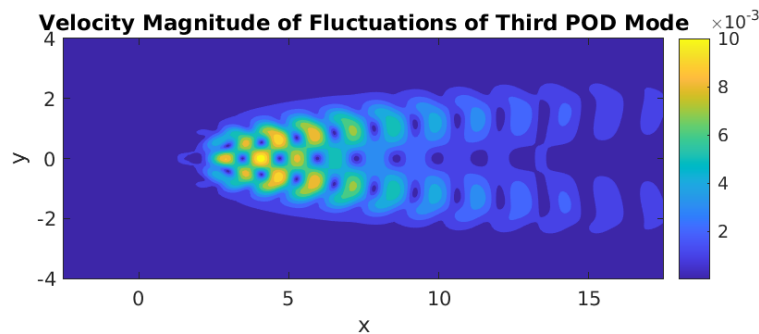


Figure 16: Second spatial POD mode for the stationary cylinder

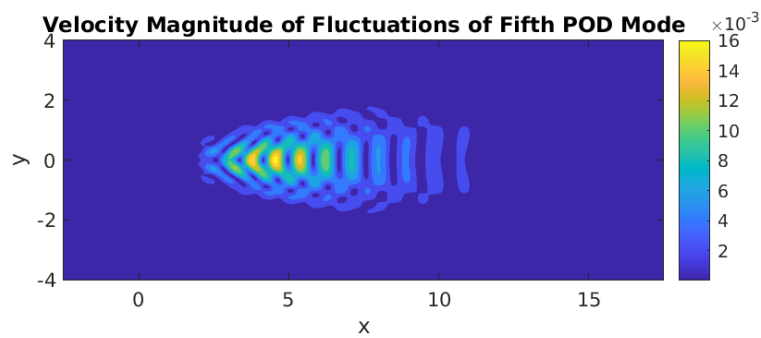


Figure 17: Third spatial POD mode for the stationary cylinder

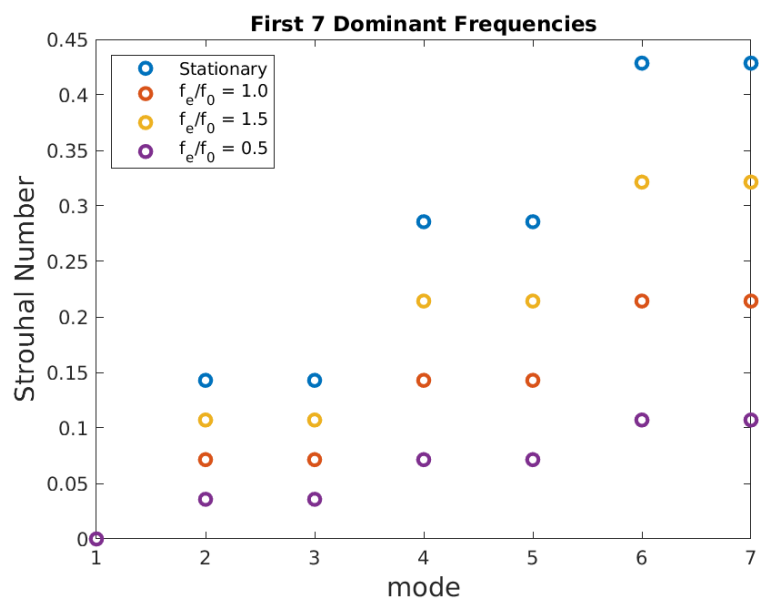


Figure 18: First seven dominant frequency derived from DMD

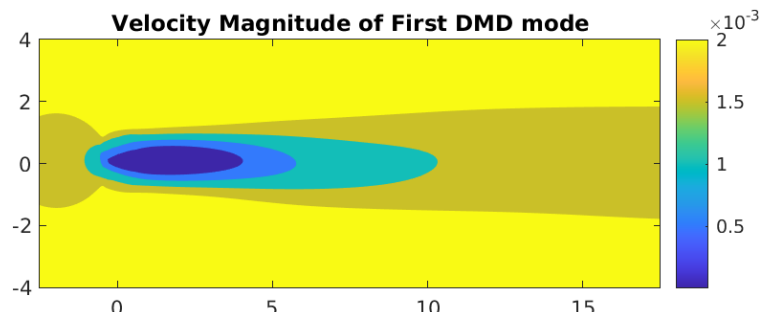


Figure 19: First spatial DMD mode for $f_e/f_0 = 1.0$

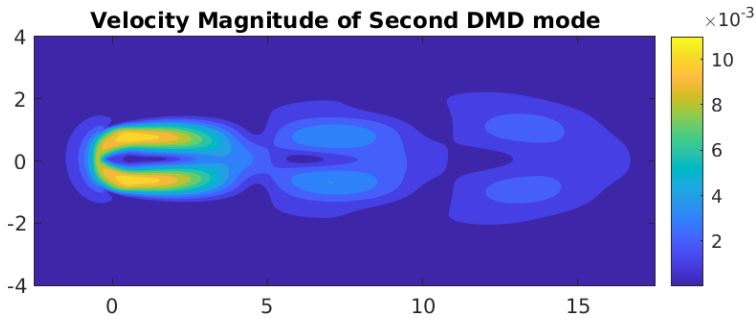


Figure 20: Second spatial DMD mode for $f_e/f_0 = 1.0$

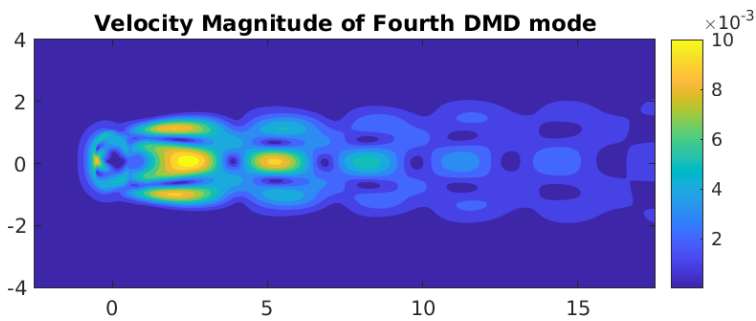


Figure 21: Fourth spatial DMD mode for $f_e/f_0 = 1.0$

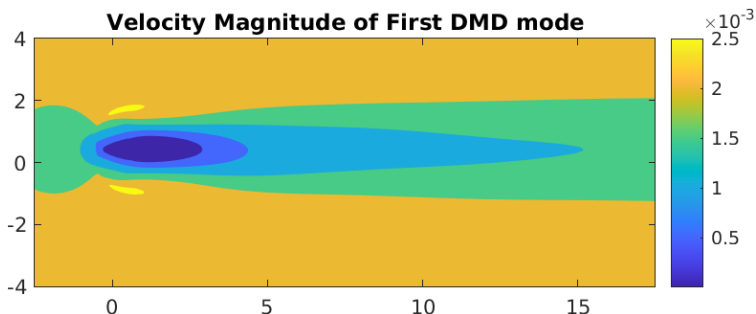


Figure 22: First spatial DMD mode for $f_e/f_0 = 1.5$

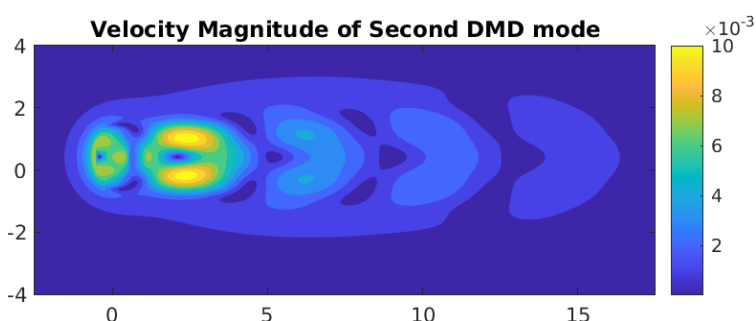


Figure 23: Second spatial DMD mode for $f_e/f_0 = 1.5$

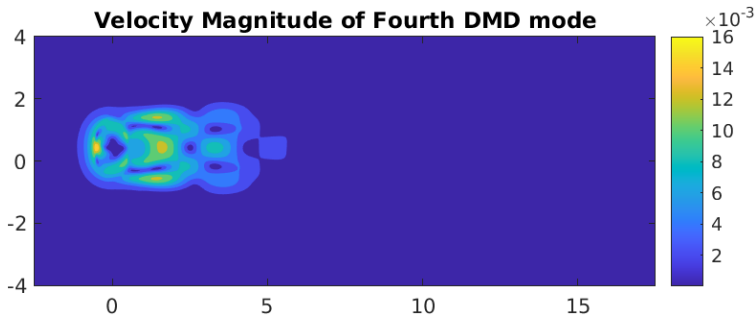


Figure 24: Fourth spatial DMD mode for $f_e/f_0 = 1.5$

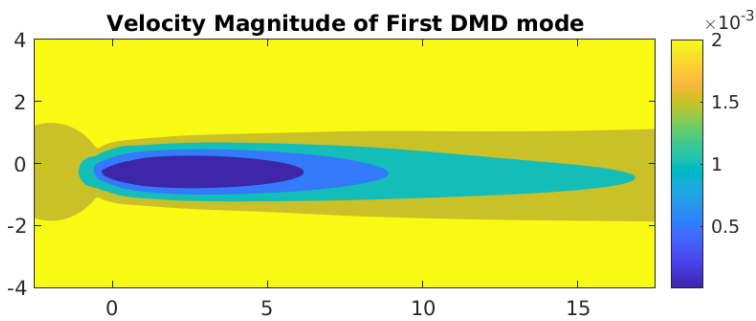


Figure 25: First spatial DMD mode for $f_e/f_0 = 0.5$

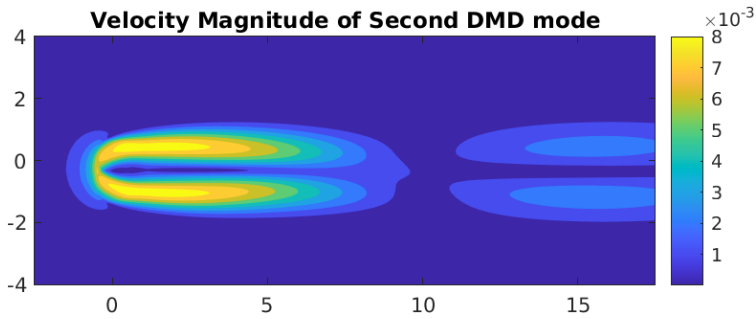


Figure 26: Second spatial DMD mode for $f_e/f_0 = 0.5$

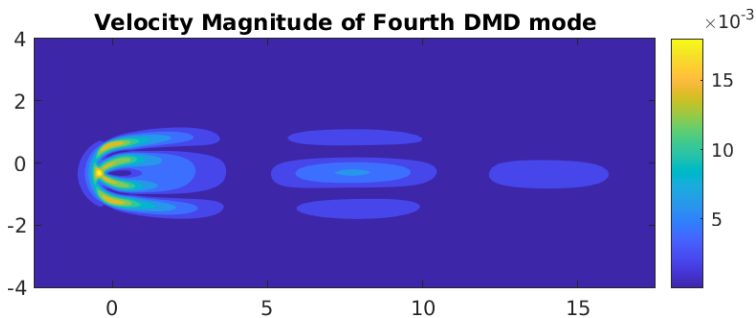


Figure 27: Fourth spatial DMD mode for $f_e/f_0 = 0.5$

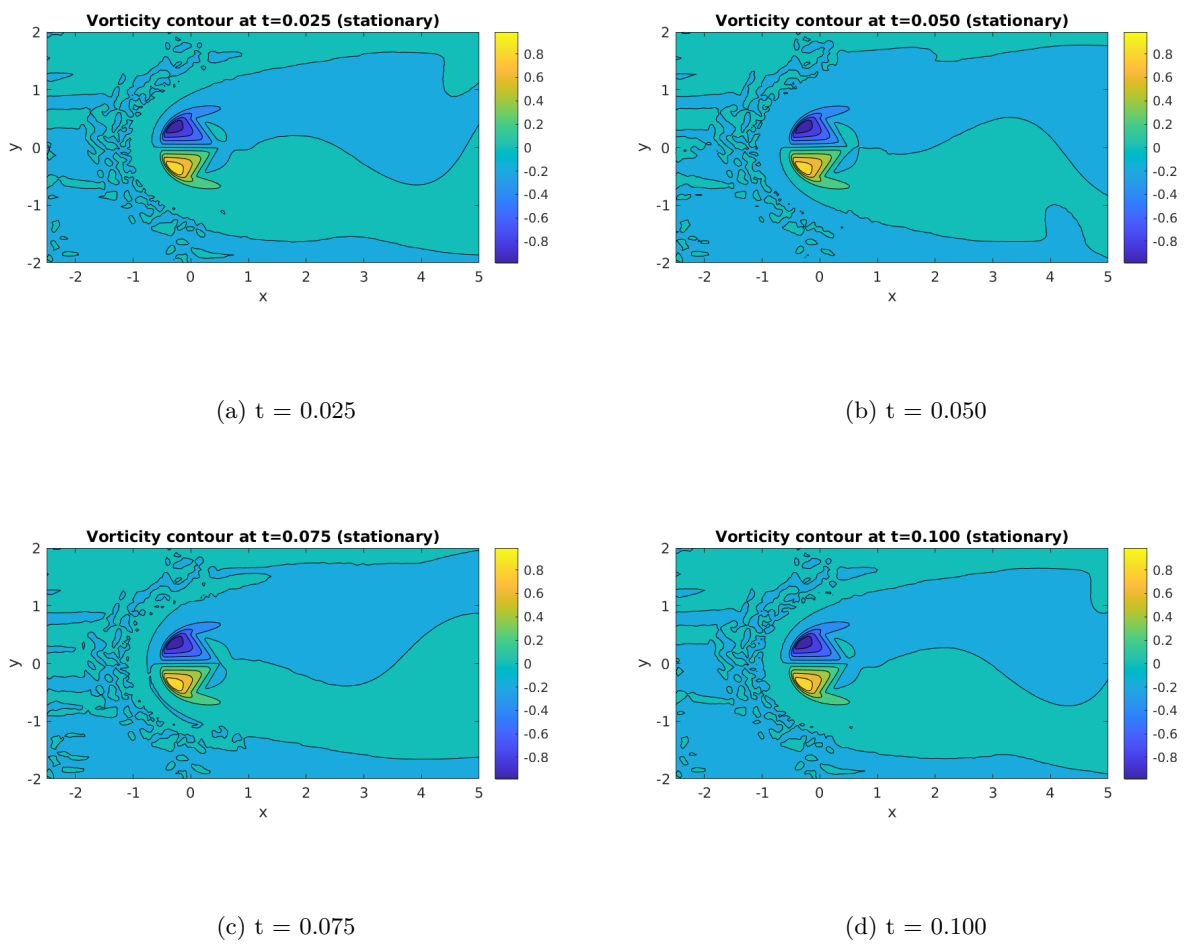
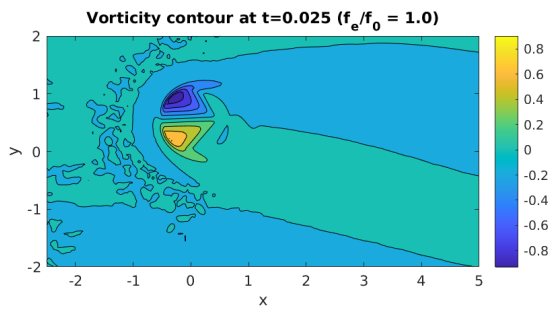
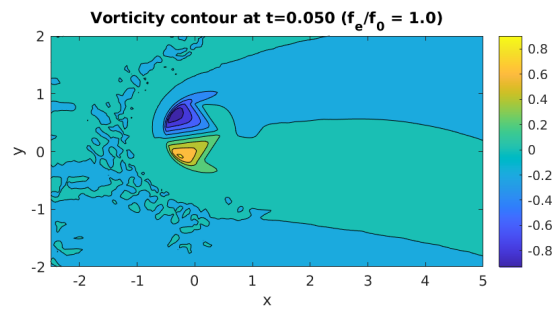


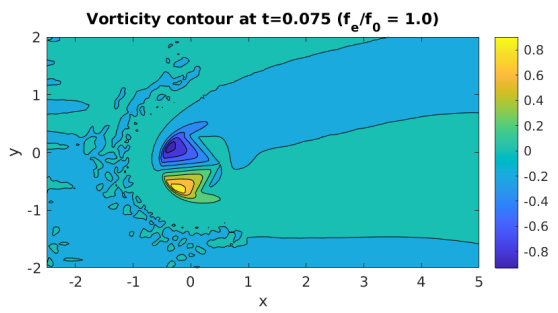
Figure 28: Vorticity contour for stationary cylinder



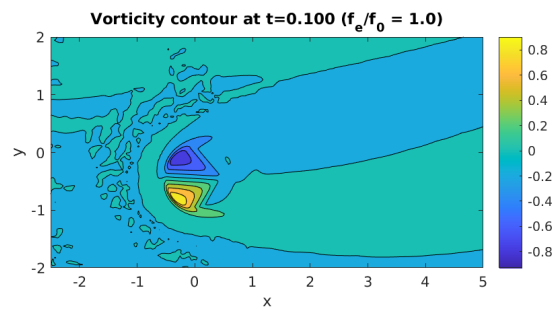
(a) $t = 0.025$



(b) $t = 0.050$

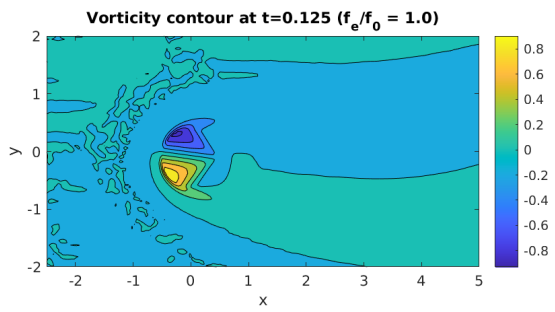


(c) $t = 0.075$

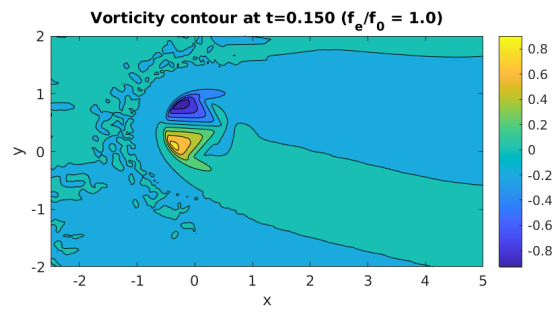


(d) $t = 0.100$

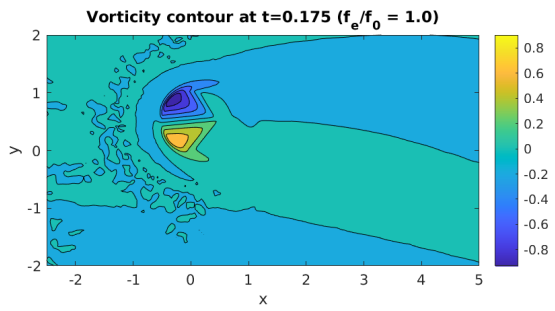
Figure 29: Vorticity contour for $f_e/f_0 = 1.0$



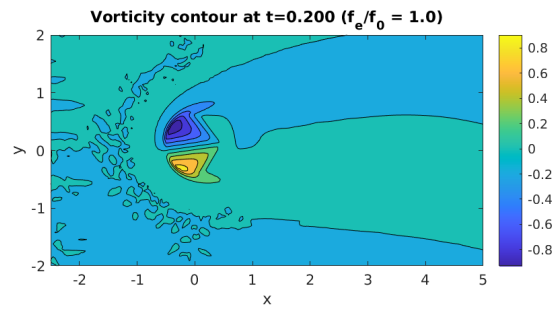
(a) $t = 0.125$



(b) $t = 0.150$



(c) $t = 0.175$



(d) $t = 0.200$

Figure 30: Vorticity contour for $f_e/f_0 = 1.0$

B Code and Animation Videos

All the code and animation videos are posted in the github repository <https://github.com/smkindo/oscillatingcylinder>.